Transition Strength Measurements to Guide Magic Wavelength Selection in Optically Trapped Molecules

K. H. Leung,[1] I. Majewska,[2] H. Bekker,[1,*] C.-H. Lee,[1,†] E. Tiberi,[1] S. S. Kondov,[1,‡] R. Moszynski,[2] and T. Zelevinsky[1,§]
[1]Department of Physics, Columbia University, 538 West 120th Street, New York, New York 10027-5255, USA
[2]Quantum Chemistry Laboratory, Department of Chemistry, University of Warsaw, Pasteura 1, 02-093 Warsaw, Poland

(Received 23 May 2020; accepted 7 September 2020; published 9 October 2020)

Optical trapping of molecules with long coherence times is crucial for many protocols in quantum information and metrology. However, the factors that limit the lifetimes of the trapped molecules remain elusive and require improved understanding of the underlying molecular structure. Here we show that measurements of vibronic line strengths in weakly and deeply bound $^{88}Sr_2$ molecules, combined with *ab initio* calculations, allow for unambiguous identification of vibrational quantum numbers. This, in turn, enables the construction of refined excited potential energy curves, informing the selection of magic wavelengths that facilitate long vibrational coherence. We demonstrate Rabi oscillations between far-separated vibrational states that persist for nearly 100 ms.

DOI: 10.1103/PhysRevLett.125.153001

The interplay of light and matter has enabled major strides in creating and controlling ultracold atoms and molecules. Exquisite control over the dense internal structure of molecules, in particular, offers promising avenues for tests of fundamental physics [1–6], cold controlled chemistry and collisions [7–12], quantum simulation [13–15], quantum computation [16–19], and compact terahertz frequency references [20]. Addressing the internal states with high fidelity necessitates the manipulation of spatial and motional degrees of freedom. For cold neutral gases, one common approach is the use of optical traps. Given two molecular states, the differential trap-induced light shifts and motional decoherence can be eliminated by tuning the frequency of the trap light close to a narrow rovibronic transition such that the dynamic polarizabilities are equal. Such magic wavelength traps were recently demonstrated to extend the vibrational [21] and rotational [22,23] coherence times of an ensemble of ultracold molecules. As with atomic lattice clocks [24,25], scattering of lattice laser light is expected to play a central role in limiting achievable interrogation times. Accurate knowledge of the molecular structure is thus a primary step in the identification of specific loss channels involved in the interaction of the molecules and the trap light. Additionally, this knowledge will help determine feasible pathways for quantum state preparation of the molecules [26–29].

In this Letter, we employ Lamb-Dicke spectroscopy in an optical lattice and state-of-the-art *ab initio* calculations to measure and predict vibronic line strengths (or transition strengths) in $^{88}Sr_2$ molecules spanning over 3 orders of magnitude. This is achieved by measuring light shifts induced by a coupling laser as it is swept across a transition of interest, resulting in avoided crossing curves from which the line strengths are extracted with minimal modeling. Taken together with lattice sideband spectroscopy, these curves additionally furnish an accurate frequency-only measurement of molecular polarizability ratios. We focus on transitions between the electronic ground potential $X^1\Sigma_g^+$ (henceforth referred to as X) and singly excited Hund's case (c) potentials $(1)0_u^+$ and $(1)1_u$ corresponding to the $^1S_0$-$^3P_1$ dissociation limit. By addressing both weakly and deeply bound states, the molecular potential energy curves are probed over a wide range of internuclear distances. We combine our measurements with spectroscopic data to construct refined potential curves for 0_u^+ and 1_u in the Morse/Long-range form and apply the results to judiciously select magic wavelengths that alleviate the impact of both frequency instability and scattering of the lattice laser on coherent molecule-light interactions. We demonstrate a superposition of far-separated vibrational states that remains coherent for a record time of nearly 100 ms.

In the Born-Oppenheimer approximation, the wave function of a diatomic molecule is a product of its electronic and rovibrational parts. The rovibrational part $|\chi_{n,\Omega}^{v,J}(R)\rangle$ is a function of the internuclear distance R and is labeled by the following quantum numbers: the electronic channel n, the vibrational number v, the total angular momentum J, and its projection onto the internuclear axis in the molecule-fixed frame Ω. Following Ref. [30], the line strength for an electric-dipole transition between the rovibrational states described by the wave functions $|\chi_{n,\Omega}^{v,J}(R)\rangle$ and $|\chi_{n',\Omega'}^{v',J'}(R)\rangle$ is given by

$$S \equiv |H_{J'M'\Omega'}^{JM\Omega}\langle\chi_{n',\Omega'}^{v',J'}(R)|d_{\Omega'-\Omega}(R)|\chi_{n,\Omega}^{v,J}(R)\rangle|^2, \quad (1)$$

where $d_{\Omega'-\Omega}(R)$ is the electronic transition dipole moment, M is the projection of the total angular momentum onto the

lab-frame Z axis, and $H^{JM\Omega}_{J'M'\Omega'}$ is the rotational factor defined in the Supplemental Material [31]. In the case of transitions driven by linearly polarized light along the quantization axis, the selection rules force $M' = M$. Equation (1) can easily be generalized to the multichannel case by introducing a sum over n, n', Ω, and Ω' before taking the absolute square. The quantity of interest that is readily accessible is the Rabi frequency

$$f_R = \frac{1}{h}\sqrt{\frac{2IS}{\epsilon_0 c}}, \tag{2}$$

which quantifies the strength of coupling between two states when driven by a laser with intensity I, leading to observable light shifts in the molecular spectra. In this study, we measure the light shifts induced either by the optical lattice, which also acts as the trap as in Fig. 1(a), or by an anti-Stokes laser as in Fig. 1(b).

In the scheme shown in Fig. 1(a), we explore the coupling of $X(v = 6, J = 0)$ to a set of $J' = 1$ resonances near the bottom of the 1_u potential well by the optical lattice. For a given lattice detuning Δ from the 1_u state and the corresponding Rabi frequency f_R, the additional light shift on $X(6, 0)$ is $f_R^2/4\Delta$ in the limit $\Delta \gg f_R$. To probe this shift, we perform two-photon Raman spectroscopy on $X(6, 0)$, shown in Fig. 2(a). We initialize our molecules in either $X(-1, 0)$ or $X(-2, 0)$ via photoassociation [31] and use $0_u^+(-4, 1)$ or $0_u^+(-5, 1)$ as the intermediate state to maximize the two-photon transition rate. The choice of initial and intermediate states does not strongly affect the measured S since the lattice is far detuned from any resonances that would shift the binding energies of these states. The Raman lasers are detuned from the intermediate state by 20 MHz, and the frequency of the first Raman leg is swept, while the second is kept fixed. Measurement of the two-photon resonance frequency at various Δ gives the expected dispersive behavior, as shown in Fig. 2(b). Transition strengths are inextricably linked to polarizability, and in the Supplemental Material [31] we show that the

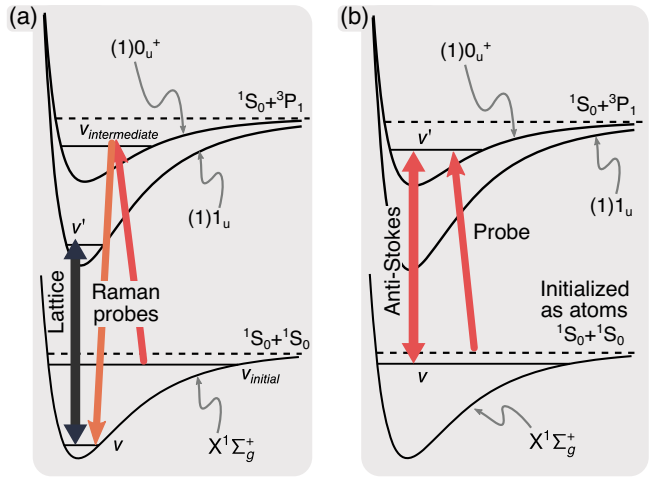

FIG. 1. Line strength measurement schemes for a pair of molecular vibrational states (v, v'). (a) For deeply bound states of 1_u, Raman spectroscopy was performed on $X^1\Sigma_g^+$ molecules initialized in near-threshold vibrational states. (b) For weakly bound states of 1_u and 0_u^+, spectroscopic probing was performed on $^1S_0$ atoms.

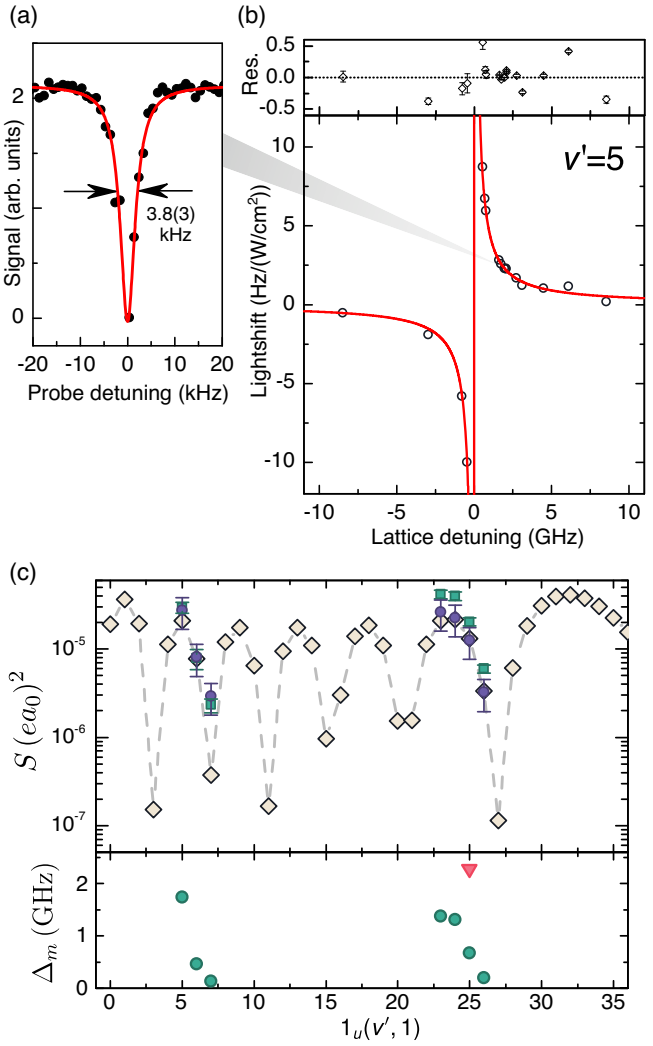

FIG. 2. (a) A two-photon Raman depletion line shape. For this trace, the differential light shift of the X states is nearly nulled, resulting in a narrow power-broadened linewidth of 3.8(3) kHz inferred from a Lorentzian fit. (b) The Raman peak locations (open circles) exhibit dispersive behavior as the lattice frequency is swept across the 1_u state (shown here for $v' = 5$). The solid red line is the fit to the avoided crossing of the form $f_R^2/4\Delta$. Residuals have units of $\mathrm{Hz}/(\mathrm{W/cm^2})$. Error bars denote 1σ uncertainties. (c) Line strengths of $X(6, 0) \to 1_u(v', 1)$ (green squares, measured and calibrated to $^1S_0$ Sr polarizability; purple circles, measured with intensity estimated from direct imaging of beam waist; yellow diamonds, calculated using the Morse potential). Also shown are the magic lattice detunings relative to the nearest 1_u state for a given pair of X states [green circles, $X(-1, 0) \to X(6, 0)$; red triangle, $X(-1, 0) \to X(4, 0)$].

ratio of f_R to the axial trap frequency of $X(-1,0)$ molecules implies that, away from any resonances, the baseline polarizability ratio of $X(6,0)$ and $X(-1,0)$ is 1.392(15) at 907.59 nm. This is then converted to absolute values of S for $X(6,0) \to 1_u(v',1)$ by calibrating to the known polarizability of $^1S_0$ atomic strontium.

Using this technique, we measure seven line strengths, where all the 1_u states are below the minimum of the 0_u^+ potential. As illustrated in Fig. 2(c), experimentally S demonstrate decreasing trends in two ranges. Prior to this Letter, we used the binding energies calculated using the *ab initio* model of Ref. [32] to assign the vibrational quantum numbers v' in the ranges 1–3 and 19–22, where we find good agreement within 0.5% of the experimental binding energies (see Table SIII in the Supplemental Material [31]). To calculate the line strengths, we model X with a set of precise empirical potential parameters obtained from the hot pipe Fourier-transform spectroscopy [48] and use the *ab initio* electronic transition dipole moment. To our surprise, the calculated *ab initio* line strengths follow the opposite trends compared to the observations, and this persisted even when the electronic transition dipole moment was modified. This suggests that the v' assignment based on the *ab initio* 1_u potential is erroneous. To overcome this, we take an alternative approach and model the short-range behavior of 1_u with the simple Morse potential

$$V(R) = D_e[1 - e^{-\beta(R-R_e)}]^2 - D_e, \tag{3}$$

where D_e is the potential depth, R_e is the equilibrium bond length, $\beta \equiv 2\pi\sqrt{2\mu\omega_e x_e c/h}$, and μ is the reduced mass of the dimer. In the presence of vibrational-rotational interaction, the energy levels are

$$E(v',J') = -D_e + \omega_e\left(v'+\frac{1}{2}\right) - \omega_e x_e\left(v'+\frac{1}{2}\right)^2 + \left[B_e - \alpha_e\left(v'+\frac{1}{2}\right)\right]J'(J'+1), \tag{4}$$

where ω_e, x_e, B_e, and α_e are the vibrational, anharmonicity, rotational, and vibration-rotation coupling spectroscopic constants, respectively. As shown in the Supplemental Material [31], the best fit of the seven observed $J'=1$ levels to Eq. (4) indicates 15 vibrational states between the two groups and $\omega_e x_e = 0.21150(28)$ cm^{-1}. Rotational spectroscopy of $J'=3$ states yields $\alpha_e = 7.068(11)\times 10^{-5}$ cm^{-1}. The Morse eigenfunctions were obtained by numerically solving the nuclear Schrödinger equation on an adaptive grid [49]. As the classical turning points of the deeply bound X states are much further apart than those of 1_u, the Frank-Condon factors for these transitions largely depend on the spatial variation of the ground-state nuclear wave function. Consequently, the calculated S versus v' exhibit a characteristic interference-like pattern with $v+1$ maxima (this rule of thumb was observed to hold up to $v \approx 12$). The measured experimental trends in S are well captured by the calculations only for v' assignments of 5–7 and 23–26 for the two ranges, as shown in Fig. 2(c) and Table SI (Supplemental Material [31]). The corresponding potential parameters are $D_e = 6387.89(11)$ cm^{-1} and $R_e = 7.9027(5)a_0$.

Hence, while the *ab initio* calculation has good accuracy in the long range, it underestimates D_e by approximately 300 cm^{-1} (5% relative difference). On the other hand, Eq. (3) allows for D_e to be empirically determined, but the simple potential cannot be extrapolated to the long range. To combine these complementary descriptions, we recast the *ab initio* 1_u and 0_u^+ potentials in the Morse/Long-range (MLR) form [33,50] and fit to spectroscopic data, while fixing D_e and R_e to their empirical values found in this Letter. In the Supplemental Material [31], we provide details of the fitting process and the MLR parameters and recalculate the energy levels of 0_u^+ and 1_u to benchmark against experimental values.

Turning to weakly bound states, an anti-Stokes laser selectively dresses $X(v, J=0)$ with a rovibrational state $0_u^+(v', J'=1)$ or $1_u(v', J'=1)$, as shown in Fig. 1(b). Here, we perform spectroscopy on a trapped sample of ultracold *atoms*. Depletion occurs when a weak probe laser is on resonance with the dressed states

$$f_\pm = \frac{\Delta}{2} \pm \frac{\sqrt{f_R^2+\Delta^2}}{2}, \tag{5}$$

where $f_+(f_-)$ is the resonance frequency of the blue-side (red-side) peak relative to the bare resonance ($f_R = 0$), and Δ is the coupling laser detuning. Figure 3(a) shows a sample trace when the anti-Stokes laser is slightly red-detuned from the $X(-2,0) \to 0_u^+(-4,1)$ transition, revealing an Autler-Townes doublet. Although the atoms are tightly confined along the axial direction of the 1D lattice, the radial confinement is much weaker. At a finite temperature of a few microkelvin, the atoms occupy several motional states above the $^1S_0 + {}^1S_0$ continuum leading to an asymmetric line shape. We determined the location of the resonances by fitting to a doublet line shape function that accounts for these thermal effects [34].

Keeping the anti-Stokes laser intensity constant, the square of the doublet separation $(f_+ - f_-)^2$ versus Δ is a parabola whose minimum is f_R^2, as shown in Fig. 3(b). This presents an attractive method of determining line strengths, as opposed to measurements involving power broadening and transition rates, since frequency differences are robust against a wide variety of effects such as reference cavity drift, the overall trap-induced light shift, shot-to-shot signal fluctuations, and the fit line shape for the doublet. Moreover, by working strictly with transitions between $J=0$ and $J'=1$ and in the regime where the anti-Stokes

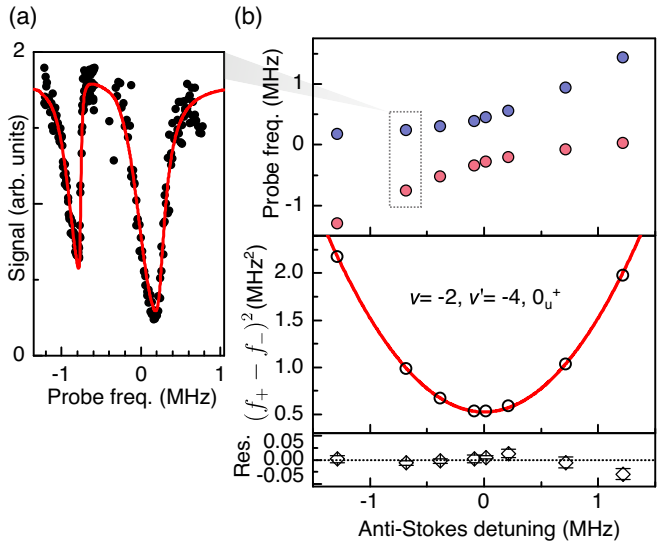

FIG. 3. (a) For a given detuning of the anti-Stokes laser from the bound-to-bound molecular transition, the probe is scanned to obtain an Autler-Townes doublet. (b) The locations of the blue-side peak (blue circles) and the red-side peak (red circles) form an avoided crossing. The square of the peak separations fit to a parabola (solid red) when plotted against the anti-Stokes detuning, the minimum of which is f_R^2. Error bars are propagated from 1σ uncertainties in the peak locations from the line shape fit. Residuals are in units of MHz^2.

detunings are larger than the Zeeman structure, the measured S are insensitive to laser polarization and are effectively between $M = M' = 0$ states. The measured S and corresponding predictions from the *ab initio* [32] and MLR models are listed in Table I. For the weakly Coriolis-mixed states, both models perform similarly well. However, for the strongly Coriolis-mixed states, only the MLR model gives the correct 0_u^+ or 1_u assignments and thus is more accurate in its predictions for S.

TABLE I. Measured (Expt.) line strengths for weakly bound 0_u^+ and 1_u states from X for various vibrational pairs. Also shown for comparison are predictions from the *ab initio* (AI) and adjusted MLR potential constructed in this Letter. Starred values are strongly Coriolis-mixed states. Statistical uncertainties account for the 1σ errors in the extracted Rabi frequencies as well as for laser power fluctuations. The units are $10^{-3}(ea_0)^2$.

$X(v, J = 0)$	State	$(v', J' = 1)$	AI	MLR	Expt.
−1	0_u^+	−4	3.09	2.77	2.57(4)
−2	0_u^+	−4	0.81	0.74	0.70(2)
−2	0_u^+	−5	5.86	5.06	4.30(6)
−3	0_u^+	−6	0.07*	8.89*	8.7(4)*
−1	1_u	−1	5.44	4.56	5.53(8)
−1	1_u	−2	0.36	0.33	0.40(1)
−2	1_u	−1	1.71	1.68	1.74(3)
−2	1_u	−2	6.95	5.82	8.0(1)
−3	1_u	−3	13.2*	2.46*	2.10(5)*

Our findings directly inform the engineering of favorable magic wavelength optical traps for a molecular clock, by means of elucidating the quantum chemistry of the strontium dimer. Just as in atomic lattice clocks, for a given baseline polarizability mismatch between the clock states, the required magic detuning Δ_m (relative to a resonance between one of the clock states and an excited state) monotonically increases with the line strength [see Fig. 2(c) and Table SI [31]]. The sensitivity of the clock transition to lattice frequency inaccuracies is simply the slope of the lattice-induced light shift at the magic detuning, $-f_R^2/4\Delta_m^2$, and would decrease monotonically for larger S (and hence larger Δ_m). Therefore, magic wavelengths based on stronger transitions place less stringent constraints on the required frequency stability of the lattice laser and on the bandwidth of the spectral filter that suppresses the lattice laser noise away from the carrier (such as amplified spontaneous emission). To this end, we compute S between

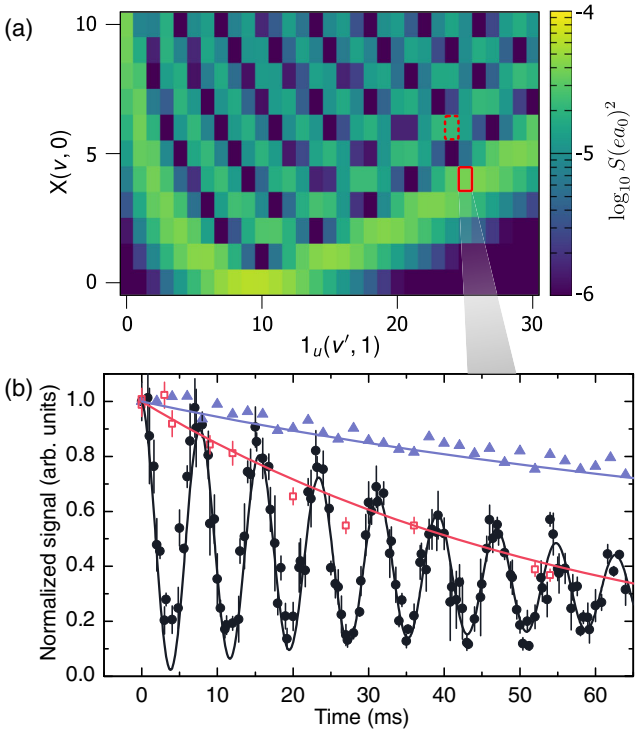

FIG. 4. (a) Line strengths of deeply bound states of 1_u to X. Solid rectangle: the transition used for the magic wavelength in this Letter. Dashed rectangle: our previous work [21]. (b) Two-photon Rabi oscillations between $X(-1, 0)$ and $X(4, 0)$ (black circles). Here, favorable magic trapping is achieved by tuning the lattice near the $X(4, 0) \rightarrow 1_u(25, 1)$ transition. Also shown are the normalized population decay of $X(4, 0)$ (red squares) and $X(-1, 0)$ (blue triangles). Black line: fit to $A\exp(-t/T_1)[1 + \exp(-t/T_2^{\text{Rabi}})\cos(\omega t - \phi)]$. Red and blue lines are fits to the rate equation $\dot{N} = -k_\gamma N^\gamma$ for the molecular number N with $\gamma = 1$ and 2, respectively, and k_γ as a free parameter. Error bars are 1σ uncertainties.

the lower-lying $J' = 1$ states of 1_u and several deeply bound $J = 0$ states of X, as shown in Fig. 4(a). For $X(4, 0)$, the state $1_u(25, 1)$ has one of the largest predicted line strengths among several v' in the vicinity. The measured magic frequency at 330.302 750 449(104) THz corresponds to a detuning $\Delta_m = 2.298(41)$ GHz from the $X(4, 0) \rightarrow 1_u(25, 1)$ resonance and is the largest studied in this Letter. Operating the molecular clock at this magic wavelength, we demonstrate long-lived two-photon Rabi oscillations [$T_2^{\mathrm{Rabi}} = 77(6)$ ms, $T_1 = 127(8)$ ms] between the clock states $X(-1, 0)$ and $X(4, 0)$, as shown in Fig. 4(b) and described in the caption. This represents a significant improvement in coherent light-molecule interactions over our previous experiment [21]. The oscillations are predominately damped by the loss of $X(4, 0)$ molecules, which has a $1/e$ lifetime of 60(2) ms at a trap depth of $k_B \times 12(1)$ μK. The single-body losses are faster for deeper traps, which indicates scattering of the lattice light. Here, analysis may be confounded by the linewidth of the lattice trap laser, since the deeply bound 1_u states are expected to be much narrower ($\Gamma_e \lesssim 2\pi \times 6$ kHz), and the situation is that of broadband scattering. Further investigations using the MLR potential curves can also help lend credence to specific loss mechanisms, such as multiphoton scattering, or to rule them out quantitatively.

In summary, we have measured the line strengths of several 0_u^+ and 1_u states connecting to the ground-state X potential in two different regimes—weakly bound near-threshold states and deeply bound states—of ultracold lattice-trapped Sr_2 molecules used in a molecular clock. The measurements were used to obtain analytic MLR potential curves for 0_u^+ and 1_u that are in good agreement with previously published binding energies and those found in this Letter. In particular, we demonstrate the reliability of the constructed 1_u potential by predicting and verifying states that have large transition strengths to X, which is an important criterion for the construction of magic optical traps. We presented an improved choice of a magic trap that led to a coherent control of the clock states for a record duration of nearly 100 ms. Furthermore, our accurate model will help elucidate the processes that contribute to the quenched molecular lifetimes and inform stimulated adiabatic pathways for ground-state preparation in future work, raising the prospects for a comprehensive vibrational spectroscopy of the ground potential as a high-precision test of molecular quantum electrodynamics and possible new physics.

We are grateful to A. Liberman and Y. Chai for contributions to the experiment. We acknowledge support from NSF Grant No. PHY-1911959 and ONR Grant No. N00014-17-1-2246. R. M. and I. M. also acknowledge the Polish National Science Center Grant No. 2016/20/W/ST4/00314.

*Present address: Helmholtz-Institut Mainz, Johannes Gutenberg University, 55128 Mainz, Germany.
†Present address: Morgan Stanley, 1585 Broadway, New York, New York 10036, USA.
‡Present address: Atom Computing, Inc., 918 Parker Street, Berkeley, California 94710, USA.
§tanya.zelevinsky@columbia.edu

[1] V. Andreev, D. G. Ang, D. DeMille, J. M. Doyle, G. Gabrielse, J. Haefner, N. R. Hutzler, Z. Lasner, C. Meisenhelder, B. R. OLeary, C. D. Panda, A. D. West, E. P. West, X. Wu (A. C. M. E. Collaboration), Improved limit on the electric dipole moment of the electron, Nature (London) **562**, 355 (2018).
[2] J. Lim, J. R. Almond, M. A. Trigatzis, J. A. Devlin, N. J. Fitch, B. E. Sauer, M. R. Tarbutt, and E. A. Hinds, Laser Cooled YbF Molecules for Measuring the Electrons Electric Dipole Moment, Phys. Rev. Lett. **120**, 123201 (2018).
[3] I. Kozyryev and N. R. Hutzler, Precision Measurement of Time-Reversal Symmetry Violation with Laser-Cooled Polyatomic Molecules, Phys. Rev. Lett. **119**, 133002 (2017).
[4] J. Kobayashi, A. Ogino, and S. Inouye, Measurement of the variation of electron-to-proton mass ratio using ultracold molecules produced from laser-cooled atoms, Nat. Commun. **10**, 3771 (2019).
[5] R. Carollo, A. Frenett, and D. Hanneke, Two-photon vibrational transitions in $^{16}O_2^+$ as probes of variation of the proton-to-electron mass ratio, Atoms **7**, 1 (2019).
[6] M. Borkowski, A. A. Buchachenko, R. Ciuryo, P. S. Julienne, H. Yamada, Y. Kikuchi, Y. Takasu, and Y. Takahashi, Weakly bound molecules as sensors of new gravitylike forces, Sci. Rep. **9**, 14807 (2019).
[7] R. V. Krems, Cold controlled chemistry, Phys. Chem. Chem. Phys. **10**, 4079 (2008).
[8] N. Balakrishnan, Perspective: Ultracold molecules and the dawn of cold controlled chemistry, J. Chem. Phys. **145**, 150901 (2016).
[9] J. L. Bohn, A. M. Rey, and J. Ye, Cold molecules: Progress in quantum engineering of chemistry and quantum matter, Science **357**, 1002 (2017).
[10] M.-G. Hu, Y. Liu, D. D. Grimes, Y.-W. Lin, A. H. Gheorghe, R. Vexiau, N. Bouloufa-Maafa, O. Dulieu, T. Rosenband, and K.-K. Ni, Direct observation of bimolecular reactions of ultracold KRb molecules, Science **366**, 1111 (2019).
[11] M. Guo, X. Ye, J. He, M. L. González-Martínez, R. Vexiau, G. Quéméner, and D. Wang, Dipolar Collisions of Ultracold Ground-State Bosonic Molecules, Phys. Rev. X **8**, 041044 (2018).
[12] M. McDonald, B. McGuyer, F. Apfelbeck, C.-H. Lee, I. Majewska, R. Moszynski, and T. Zelevinsky, Photodissociation of ultracold diatomic strontium molecules with quantum state control, Nature (London) **535**, 122 (2016).
[13] J. A. Blackmore, L. Caldwell, P. D. Gregory, E. M. Bridge, R. Sawant, J. Aldegunde, J. Mur-Petit, D. Jaksch, J. M. Hutson, B. Sauer, M. R. Tarbutt, and S. L. Cornish, Ultracold molecules for quantum simulation: Rotational coherences in CaF and RbCs, Quantum Sci. Tech. **4**, 014010 (2018).

[14] E. Altman, K. R. Brown, G. Carleo, L. D. Carr, E. Demler, C. Chin, B. DeMarco, S. E. Economou, M. Eriksson, K.-M. C. Fu *et al.*, Quantum simulators: Architectures and opportunities, arXiv:1912.06938.

[15] A. Micheli, G. K. Brennen, and P. Zoller, A toolbox for lattice-spin models with polar molecules, Nat. Phys. **2**, 341 (2006).

[16] K.-K. Ni, T. Rosenband, and D. D. Grimes, Dipolar exchange quantum logic gate with polar molecules, Chem. Sci. **9**, 6830 (2018).

[17] E. R. Hudson and W. C. Campbell, Dipolar quantum logic for freely rotating trapped molecular ions, Phys. Rev. A **98**, 040302(R) (2018).

[18] M. Hughes, M. D. Frye, R. Sawant, G. Bhole, J. A. Jones, S. L. Cornish, M. R. Tarbutt, J. M. Hutson, D. Jaksch, and J. Mur-Petit, Robust entangling gate for polar molecules using magnetic and microwave fields, Phys. Rev. A **101**, 062308 (2020).

[19] P. Yu, L. W. Cheuk, I. Kozyryev, and J. M. Doyle, A scalable quantum computing platform using symmetric-top molecules, New J. Phys. **21**, 093049 (2019).

[20] C. Wang, X. Yi, J. Mawdsley, M. Kim, Z. Wang, and R. Han, An on-chip fully electronic molecular clock based on sub-terahertz rotational spectroscopy, National electronics review **1**, 421 (2018).

[21] S. S. Kondov, C.-H. Lee, K. H. Leung, C. Liedl, I. Majewska, R. Moszynski, and T. Zelevinsky, Molecular lattice clock with long vibrational coherence, Nat. Phys. **15**, 1118 (2019).

[22] R. Bause, M. Li, A. Schindewolf, X.-Y. Chen, M. Duda, S. Kotochigova, I. Bloch, and X.-Y. Luo, Tune-Out and Magic Wavelengths for Ground-State $^{23}Na^{40}K$ Molecules, Phys. Rev. Lett. **125**, 023201 (2020).

[23] F. Seeßelberg, X.-Y. Luo, M. Li, R. Bause, S. Kotochigova, I. Bloch, and C. Gohle, Extending Rotational Coherence of Interacting Polar Molecules in a Spin-Decoupled Magic Trap, Phys. Rev. Lett. **121**, 253401 (2018).

[24] R. B. Hutson, A. Goban, G. E. Marti, L. Sonderhouse, C. Sanner, and J. Ye, Engineering Quantum States of Matter for Atomic Clocks in Shallow Optical Lattices, Phys. Rev. Lett. **123**, 123401 (2019).

[25] S. Dörscher, R. Schwarz, A. Al-Masoudi, S. Falke, U. Sterr, and C. Lisdat, Lattice-induced photon scattering in an optical lattice clock, Phys. Rev. A **97**, 063419 (2018).

[26] J. W. Park, S. A. Will, and M. W. Zwierlein, Two-photon pathway to ultracold ground state molecules of $^{23}Na^{40}K$, New J. Phys. **17**, 075016 (2015).

[27] M. Guo, R. Vexiau, B. Zhu, B. Lu, N. Bouloufa-Maafa, O. Dulieu, and D. Wang, High-resolution molecular spectroscopy for producing ultracold absolute-ground-state $^{23}Na^{87}Rb$ molecules, Phys. Rev. A **96**, 052505 (2017).

[28] K. Aikawa, D. Akamatsu, M. Hayashi, J. Kobayashi, M. Ueda, and S. Inouye, Predicting and verifying transition strengths from weakly bound molecules, Phys. Rev. A **83**, 042706 (2011).

[29] A. Ciamei, A. Bayerle, C.-C. Chen, B. Pasquiou, and F. Schreck, Efficient production of long-lived ultracold Sr_2 molecules, Phys. Rev. A **96**, 013406 (2017).

[30] A. Hansson and J. K. Watson, A comment on Hnl-London factors, J. Mol. Spectrosc. **233**, 169 (2005).

[31] See Supplemental Material at http://link.aps.org/supplemental/10.1103/PhysRevLett.125.153001 for details on the experimental methods, determination of the spectroscopic constants, the best fit potential parameters of the Morse/Long-range potentials, and additional data, which includes Refs. [22,32–47].

[32] W. Skomorowski, F. Pawowski, C. P. Koch, and R. Moszynski, Rovibrational dynamics of the strontium molecule in the $A^1\Sigma_u^+$, $c^3\Pi_u$, and $a^3\Sigma_u^+$ manifold from state-of-the-art *ab initio* calculations, J. Chem. Phys. **136**, 194306 (2012).

[33] R. J. Le Roy, N. S. Dattani, J. A. Coxon, A. J. Ross, P. Crozet, and C. Linton, Accurate analytic potentials for $Li_2(X^1\Sigma_g^+)$ and $Li_2(A^1\Sigma_u^+)$ from 2 to 90 Å, and the radiative lifetime of $Li(2p)$, J. Chem. Phys. **131**, 204309 (2009).

[34] B. McGuyer, M. McDonald, G. Z. Iwata, M. Tarallo, A. Grier, F. Apfelbeck, and T. Zelevinsky, High-precision spectroscopy of ultracold molecules in an optical lattice, New J. Phys. **17**, 055004 (2015).

[35] G. Reinaudi, C. B. Osborn, M. McDonald, S. Kotochigova, and T. Zelevinsky, Optical Production of Stable Ultracold $^{88}Sr_2$ Molecules, Phys. Rev. Lett. **109**, 115303 (2012).

[36] J. Stenger, H. Schnatz, C. Tamm, and H. R. Telle, Ultraprecise Measurement of Optical Frequency Ratios, Phys. Rev. Lett. **88**, 073601 (2002).

[37] N. Scharnhorst, J. B. Wübbena, S. Hannig, K. Jakobsen, J. Kramer, I. D. Leroux, and P. O. Schmidt, High-bandwidth transfer of phase stability through a fiber frequency comb, Opt. Express **23**, 19771 (2015).

[38] M. McDonald, B. H. McGuyer, G. Z. Iwata, and T. Zelevinsky, Thermometry via Light Shifts in Optical Lattices, Phys. Rev. Lett. **114**, 023001 (2015).

[39] B. H. McGuyer, M. McDonald, G. Z. Iwata, M. G. Tarallo, W. Skomorowski, R. Moszynski, and T. Zelevinsky, Precise study of asymptotic physics with subradiant ultracold molecules, Nat. Phys. **11**, 32 (2015).

[40] S. G. Porsev, A. D. Ludlow, M. M. Boyd, and J. Ye, Determination of Sr properties for a high-accuracy optical clock, Phys. Rev. A **78**, 032508 (2008).

[41] I. Ushijima, M. Takamoto, and H. Katori, Operational Magic Intensity for Sr Optical Lattice Clocks, Phys. Rev. Lett. **121**, 263202 (2018).

[42] M. Borkowski, P. Morzyński, R. Ciuryło, P. S. Julienne, M. Yan, B. J. DeSalvo, and T. C. Killian, Mass scaling and nonadiabatic effects in photoassociation spectroscopy of ultracold strontium atoms, Phys. Rev. A **90**, 032713 (2014).

[43] S. G. Porsev, M. S. Safronova, and C. W. Clark, Relativistic calculations of C_6 and C_8 coefficients for strontium dimers, Phys. Rev. A **90**, 052715 (2014).

[44] J. Mitroy and J. Zhang, Dispersion and polarization interactions of the strontium atom, Mol. Phys. **108**, 1999 (2010).

[45] G. Ferrari, P. Cancio, R. Drullinger, G. Giusfredi, N. Poli, M. Prevedelli, C. Toninelli, and G. M. Tino, Precision Frequency Measurement of Visible Intercombination Lines of Strontium, Phys. Rev. Lett. **91**, 243002 (2003).

[46] M. McDonald, *High Precision Optical Spectroscopy and Quantum State Selected Photodissociation of Ultracold $^{88}Sr_2$ Molecules in an Optical Lattice* (Springer, New York, 2017).

[47] T. Zelevinsky, M. M. Boyd, A. D. Ludlow, T. Ido, J. Ye, R. Ciuryło, P. Naidon, and P. S. Julienne, Narrow Line Photoassociation in an Optical Lattice, Phys. Rev. Lett. **96**, 203201 (2006).

[48] A. Stein, H. Knckel, and E. Tiemann, The $^1S + {}^1S$ asymptote of Sr_2 studied by Fourier-transform spectroscopy, Eur. Phys. J. D **57**, 171 (2010).

[49] E. Tiesinga, C. J. Williams, and P. S. Julienne, Photoassociative spectroscopy of highly excited vibrational levels of alkali-metal dimers: Green-function approach for eigenvalue solvers, Phys. Rev. A **57**, 4257 (1998).

[50] R. J. Le Roy and R. D. Henderson, A new potential function form incorporating extended long-range behaviour: Application to ground-state Ca_2, Mol. Phys. **105**, 663 (2007).

Transition strength measurements to guide magic wavelength selection in optically trapped molecules: Supplemental Material

K. H. Leung,[1] I. Majewska,[2] H. Bekker,[1,*] C.-H. Lee,[1,†] E. Tiberi,[1] S. S. Kondov,[1,‡] R. Moszynski,[2] and T. Zelevinsky[1,§]

[1] *Department of Physics, Columbia University, 538 West 120th Street, New York, NY 10027-5255, USA*
[2] *Quantum Chemistry Laboratory, Department of Chemistry, University of Warsaw, Pasteura 1, 02-093 Warsaw, Poland*

This supplement describes the experimental setup and expounds on the procedure in determining the spectroscopic constants of $(1)1_u$, and the Morse/Long-range potential parameters for $(1)0_u^+$ and $(1)1_u$. We also present additional data on the magic detunings, and binding energies of the deeply bound 1_u states discovered in this work.

DEFINITION OF THE ROTATIONAL FACTOR

The rotational factor in the expression for line strength in the main text is defined as

$$H^{JM\Omega}_{J'M'\Omega'} \equiv (-1)^{M-\Omega}\sqrt{(2J+1)(2J'+1)} \times \sqrt{1+\delta_{\Omega 0}+\delta_{\Omega' 0}-2\delta_{\Omega 0}\delta_{\Omega' 0}} \times \begin{pmatrix} J & 1 & J' \\ M & 0 & -M' \end{pmatrix} \begin{pmatrix} J & 1 & J' \\ \Omega & \Omega'-\Omega & \Omega' \end{pmatrix}. \tag{S1}$$

EXPERIMENTAL SETUP

A detailed account of our experimental setup has been given elsewhere [S1]. Briefly, ^{88}Sr atoms are laser-cooled in a two-stage magneto-optical trap (MOT) operating on the strong $^1S_0$-$^1P_1$ transition at 461 nm and the spin-forbidden intercombination transition $^1S_0$-$^3P_1$ at 689 nm, producing over 10^4 atoms in the $^1S_0$ electronic ground state at a final temperature of approximately $4(1)\,\mu$K as measured from a ballistic expansion of the gas. The atoms are transferred to a horizontal one-dimensional optical lattice with a typical trap depth of $50\,\mu$K and axial confinement frequency of 70 kHz such that spectroscopy near the intercombination line is in the Lamb-Dicke and resolved sideband regimes. Note that for the data demonstrating Rabi oscillations, we used a lower trap depth of $12\,\mu$K to prolong the lifetime of the deeply bound X state.

We can efficiently produce weakly bound vibrational states belonging to the ground potential, X, by photoassociating to a weakly bound 0_u^+ state where a reasonably strong spontaneous decay pathway to X exists owing to favorable Franck-Condon overlap. Depending on the molecular transition of interest, we perform spectroscopy on a sample of either ultracold strontium atoms or molecules. We count the number of atoms remaining in $^1S_0$ after a spectroscopy sequence by absorption imaging on the $^1S_0$-$^1P_1$ transition (a molecular sample is first photodissociated into atoms).

The photoassociation, photodissociation, and probe laser beams are phase-locked to a sub-kHz linewidth master laser that is itself stabilized to a high-finesse reference cavity ($\mathcal{F} \sim 30{,}000$). The Raman lasers are co-stabilized with an erbium-doped fiber-based optical frequency comb using the transfer-oscillator technique [S2, S3]. The repetition rate of the frequency comb is phase-locked to the master laser, while its carrier offset is referenced to a GPS guided Rb frequency standard. For the coherent Rabi oscillations, the lattice is phase-locked to the frequency comb. All laser beams are coaligned with the lattice and focused onto the atoms or molecules.

OPTICAL BEAM MODELING

To determine the spatial profile of the light shift inducing laser beam (either the anti-Stokes or the optical lattice), we deflect the beams just before the viewport of the vacuum chamber onto a camera (Thorlabs DCC1545M) positioned at the focal plane of the forward-pass lattice beam. Typically, the waist of the lattice beam is $< 50\,\mu$m, and that of the anti-Stokes is much larger at $100\,\mu$m. The pixel size of the camera is $5.2\,\mu\text{m} \equiv h$.

In the measurements involving weakly bound states, to account for any possible misalignment of the anti-Stokes and any non-idealities in its spatial profile, the local intensity experienced by the molecules is estimated as the intensity in one square pixel at the position of the lattice on the camera. This was achieved by obtaining a conversion ratio between the total count read by all camera pixels (C_{tot}) to the total optical power received on a power meter (P) in the same optical path. The local intensity is thus

$$\frac{P}{C_{\text{tot}}}\frac{C_{\text{local}}}{h^2}, \tag{S2}$$

where C_{local} is the pixel count at the lattice position. For an ideal Gaussian beam with waist w_0, this method systematically underestimates the intensity near the peak

due to the finite pixel size by a factor

$$\frac{\pi}{2}\left[\frac{w_0}{h}\mathrm{erf}\left(\frac{h}{\sqrt{2}w_0}\right)\right]^2. \tag{S3}$$

For our parameters, this error propagates into the line strength at the 0.01% level and is negligible compared to the statistical error arising from the measurement of the Rabi frequency and the optical power.

In the measurements involving deeply bound states, the lattice laser itself induces the light shift. In one method, we estimate the intensity of the lattice by directly imaging and fitting a Gaussian spatial profile to the focused forward-pass lattice beam to extract its beam waist, w_{latt}. This sets an upper limit for the lattice intensity, as experimental imperfections tend to degrade the quality of the optical standing wave. These include imperfect wavefront matching of the retroreflected beam with the forward beam, losses and aberration due to optical elements in the beam path, and the overlap location of the MOT and the lattice. Over a time scale of approximately a year, during which the data in this work was collected, we noticed a variance by a factor of approximately $\sqrt{2}$ in the axial sideband frequency determined by optically probing the blue and red axial sidebands of the narrow subradiant transition from $\mathrm{X}(v=-1, J=0)$ to $1_g(v'=-1, J'=1)$ [S4, S5]. We attribute this to long-term thermal or mechanical instability of elements in the beam path and ambient magnetic field drifts which would shift the MOT-lattice overlap position. We thus define an effective waist, w_{eff}, such that $w_{\mathrm{latt}} \lesssim w_{\mathrm{eff}} \lesssim \sqrt{2}w_{\mathrm{latt}}$, and take the average and range as the value and uncertainty for w_{eff} respectively. The local intensity, in this method, is estimated as

$$\frac{8P_f}{\pi w_{\mathrm{eff}}^2}, \tag{S4}$$

where P_f is the optical power of the forward beam. For the deeply bound $X \rightarrow 1_u$ transition strengths reported using this method (purple circles in Fig. 2 (c)), we used $w_{\mathrm{eff}} = 42(7)$ μm.

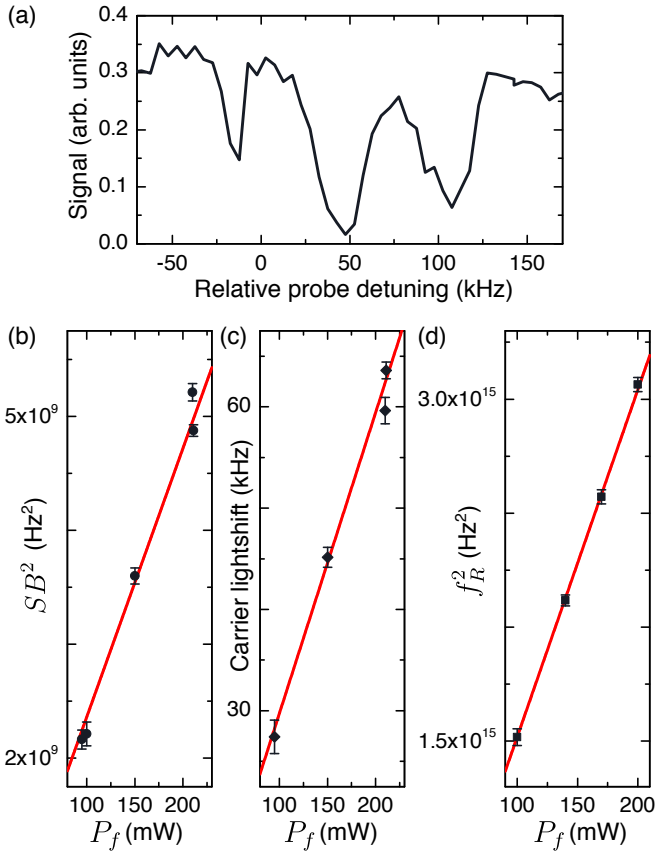

Figure S1. (a) Sample spectrum of the narrow single-photon subradiant transition $\mathrm{X}(-1,0) \rightarrow 1_g(-1,1)$ which has an intrinsic linewidth of < 100 Hz, showing the axial red sideband, carrier, and blue sideband as a function of increasing probe frequency. (b) Square of the raw spectroscopic sideband separation, SB, defined as half the frequency difference of the blue and red sidebands, plotted against the power of the forward lattice beam, P_f. (c) As the spectroscopy was not performed at the magic wavelength of the subradiant transition, the carrier exhibits a differential light shift. The slope of the linear fit, L_0, is used to correct SB^2/P_f to obtain the true axial sideband frequency of the $\mathrm{X}(-1,0)$ molecules: $f_{\mathrm{ax}}^2/P_f = SB^2/P_f + 2hL_0/(M\lambda^2)$. (d) f_R^2 obtained from the dispersive avoided crossings at various P_f, shown here for $\mathrm{X}(4,0) \rightarrow 1_u(25,1)$. The ratio of the slopes of f_R^2/P_f and f_{ax}^2/P_f provides an accurate method to determine the polarizability ratio for the clock states, independent of the local trap intensity experienced by the molecules. This, in turn, is converted to a $\mathrm{X} \rightarrow 1_u$ transition strength using the known atomic polarizability of Sr.

CALIBRATION OF TRANSITION STRENGTHS TO KNOWN ATOMIC POLARIZABILITY

In this section, we present an alternative, frequency-based method of extracting the deeply bound $\mathrm{X} \rightarrow 1_u$ transition strengths based on calibrating the intensity experienced by the molecules to a known polarizability value.

In the vicinity of a narrow resonance to an electronically excited molecular state such as $1_u(v',1)$, the dynamic polarizability of the deeply bound ground vibrational state $\mathrm{X}(v,0)$ can be written as the sum of a resonant contribution and a background, or baseline, term:

$$\alpha_v = -\frac{1}{h}\frac{S}{\Delta} + \alpha_v^{bg}, \tag{S5}$$

where S is the transition strength between the deeply bound ground state and the excited state, and Δ is the corresponding frequency detuning from resonance [S6]. In this work, $v = 4$ or 6. Since we deal exclusively with $J = 0$ ground state molecules, the polarizability

is a scalar quantity. The polarizability, α_{-1}, of the initial state X$(-1,0)$ from which we perform Raman spectroscopy, and the baseline term α_v^{bg}, are largely unperturbed as the lattice is swept across the 1_u resonance. The clock-state differential polarizability, $\alpha_v - \alpha_{-1}$, is nulled at the magic detuning Δ_m, and it follows from Eq. (S5) that

$$\alpha_v^{bg} - \alpha_{-1} = \frac{1}{h}\frac{S}{\Delta_m}. \tag{S6}$$

Experimentally, we have access to the Rabi frequency $f_R^2 = (2S/h^2)(I/\epsilon_0 c)$ from the avoided crossings as described in the main text. Additionally, by optically probing the blue and red axial sidebands of the narrow subradiant transition X$(-1,0) \rightarrow 1_g(-1,1)$, we can obtain the axial trap frequency for X$(-1,0)$ molecules, $f_{\rm ax}$, which is related to α_{-1} by

$$f_{\rm ax}^2 = \alpha_{-1}\frac{1}{M\lambda^2}\frac{I}{\epsilon_0 c}, \tag{S7}$$

where λ is the lattice wavelength at which the sideband measurement was performed and M is the molecular mass [S4, S5]. Thus, the following frequency ratio is independent of beam intensity:

$$\frac{f_R^2}{f_{\rm ax}^2} = \frac{1}{E_R}\frac{S}{\alpha_{-1}} = \frac{\Delta_m}{E_R/h}\left(\frac{\alpha_v^{bg}}{\alpha_{-1}} - 1\right), \tag{S8}$$

where $E_R = \frac{h^2}{2M\lambda^2}$ is the recoil energy and in the last step we substituted Eq. (S6). This provides a method to accurately and precisely determine the polarizability ratio using only frequency measurements.

It is important that the lattice is tuned near the wavelength of the X$(v,0) \rightarrow 1_u(v',1)$ resonance when performing the X$(-1,0) \rightarrow 1_g(-1,1)$ single-photon sideband measurement so that α_{-1} is kept the same as in the experiment to determine f_R^2. The spectroscopic separation of the sidebands is corrected to take into account the differential light shift of the subradiant transition using the carrier peak, thereby allowing for an accurate measurement of the axial trap frequency for X$(-1,0)$ molecules even though the subradiant transition itself is non-magic. This is illustrated in Fig. S1. To reject common-mode systematic errors and ensure the same experimental conditions, we measure $f_{\rm ax}^2$ immediately after f_R^2.

We apply this technique of measuring baseline polarizability ratios to find $\alpha_4^{bg}/\alpha_{-1} = 1.366(10)$ and $\alpha_6^{bg}/\alpha_{-1} = 1.392(15)$ at $\lambda = 907.64$ nm and 907.59 nm, respectively. From Eq. (S6), we see that together with the measured magic detunings, these accurate polarizability ratios can be converted into transition strengths using the well known polarizability of the $^1S_0$ atomic state $\alpha_{\rm Sr}$ as a reference:

$$S \simeq 2\alpha_{\rm Sr}\left(\frac{\alpha_v^{bg}}{\alpha_{-1}} - 1\right)h\Delta_m. \tag{S9}$$

Here we used $\alpha_{-1} \simeq 2\alpha_{\rm Sr}$ which is a valid approximation since X(-1,0) is bound by less than 137 MHz. Put another way, this method calibrates the lattice intensity using the known atomic polarizability.

In Table SI, we list the transition strengths of the X$(v,0) \rightarrow 1_u(v',1)$ resonances obtained in three ways: (1) using the experimental polarizability ratios, (2) using the estimated beam waist $w_{\rm eff}$ as described in the preceding section, and (3) via a theoretical calculation using the Morse/Long-range potential. For X$(v = 4-6, 0) \rightarrow 1_u(v' = 23-26, 1)$ in the 907-925 nm wavelength range, we use $\alpha_{\rm Sr} = 261.2$ a.u. at 914 nm [S7]. Owing to practical reasons, for X$(v = 6, 0) \rightarrow 1_u(v' = 5-7, 1)$ we partially turn to a molecular polarizability calculation for the X states using the sum-over-states method with *ab initio* transition moments. We estimate that the polarizability of X$(-1,0)$ is $\alpha_{-1} \simeq 2\alpha_{\rm Sr} = 2 \times 236$ a.u. at 1045–1063 nm, and in the same range the experimental value for $\alpha_6^{bg}/\alpha_{-1}$ should be scaled by a factor of 0.89(9), to obtain 1.239(25). Here we quote an uncertainty of 10% on this scale factor based on the expected accuracy of the *ab initio* transition moment of the deeply bound X state to the higher-lying potentials asymptoting to $^3P_1 + {}^3P_1$. As a benchmark, our polarizability calculations predict $\alpha_{-1} = 2 \times 256$ a.u. and 2×282 a.u. at 914 nm and 813.4 nm, respectively, matching to within a few atomic units the values calculated [S7] and experimentally measured [S8] for $\alpha_{\rm Sr}$.

SPECTROSCOPIC CONSTANTS OF THE 1_u POTENTIAL

The energy spectrum of the simple Morse potential with vibration-rotation coupling is

$$E(v',J') = -D_e + \omega_e\left(v'+\frac{1}{2}\right) - \omega_e x_e\left(v'+\frac{1}{2}\right)^2 + \left[B_e - \alpha_e\left(v'+\frac{1}{2}\right)\right]J'(J'+1), \tag{S10}$$

where ω_e, x_e, B_e and α_e are the vibrational, anharmonicity, rotational and vibration-rotation coupling spectroscopic constants respectively.

To find α_e, we measure the rotational splitting of $J' = 3$ and 1 for various v'. Using Eq. (S10), we see that

$$E(v',3) - E(v',1) = 10B_e - 10\alpha_e\left(v'+\frac{1}{2}\right), \tag{S11}$$

so that plotted against $v' + \frac{1}{2}$ the slope of the linear fit is $-10\alpha_e$ and insensitive to an overall offset in the v' labels. In order to address both $J' = 3$ and 1, we populate X$(v = 6, J = 2)$ with a long stimulated Raman pulse from X$(v = -1, J = 0)$ in a non-magic lattice. Then, a short probe pulse ($\sim 100\,\mu$s) resonant with either J' state

Table SI. List of measured deeply bound transition strengths of $X(v,0) \to 1_u(v',1)$, the respective magic detunings and resonant wavelengths. For precise values of the binding energies of the 1_u states, see Table SIII. Except for $X(6,0) \to 1_u(25,1)$, the initial state of the Raman transition is always $X(-1,0)$.

Raman transition $X(v_{initial},0) \to X(v,0)$	$1_u(v',1)$	λ (nm)	Δ_m (GHz)	$S\,(10^{-5}\,(ea_0)^2)$		
				Calibrated to α_{Sr}	Direct beam waist	Theory
$-1 \to 6$	26	907.587	0.195(2)	0.601(65)	0.32(13)	0.336
$-2 \to 6$	25	913.597	0.670(18)	2.08(23)	1.25(49)	1.32
$-1 \to 6$	24	919.725	1.316(1)	4.09(44)	2.27(89)	2.16
$-1 \to 6$	23	925.973	1.380(2)	4.29(46)	2.6(1.0)	2.10
$-1 \to 6$	7	1045.233	0.135(14)	0.231(41)	0.29(12)	0.0375
$-1 \to 6$	6	1054.101	0.46(10)	0.79(21)	0.81(32)	0.779
$-1 \to 6$	5	1063.185	1.743(13)	2.98(43)	2.8(1.1)	2.09
$-1 \to 4$	25	907.636	2.298(41)	6.68(70)	9.4(3.2)	3.88

Table SII. Rotational splitting (in units of GHz) between $J' = 3$ and $J' = 1$ for a given v' state of 1_u.

v'	$E(v',3) - E(v',1)$
23	6.07728(9)
24	6.05616(9)
26	6.01375(6)

depletes the population. Finally, we perform another Raman pulse to transfer the population back to $X(-1,0)$ where it is dissociated and detected. The Raman transfer is inefficient owing to the polarizability mismatch, but we nevertheless obtain sufficient signal to perform the spectroscopy. We vary the optical lattice power between two extremes and linearly extrapolate to zero power to obtain the resonance frequency. The absolute frequency of a resonant probe pulse was determined using an optical frequency comb. Table SII lists the measured rotational splittings for three states, and Fig. S2(a) shows the linear fit from which we extract $\alpha_e = 7.068(11) \times 10^{-5}\,\mathrm{cm}^{-1}$.

To determine $\omega_e x_e$, we take differences of adjacent vibrational energy levels for $J' = 1$. Eq. (S10) suggests that

$$E(v'+1,1) - E(v',1) = (\omega_e - 2\alpha_e) - 2\omega_e x_e (v'+1). \quad \text{(S12)}$$

Therefore, plotting this difference against $v'+1$ should yield a straight line with a slope equal to $-2\omega_e x_e$ that is similarly insensitive to an overall offset in the v' labels (Fig. S2(b)). The best fits, judged on the basis of the reduced χ^2, are obtained if there are 15 intermediate vibrational states in the region where data is absent. We thus obtain $\omega_e x_e = 0.21150(28)\,\mathrm{cm}^{-1}$.

Note that for the linear fits in Fig. S2 (a) and (b), the vertical intercepts are $10B_e$ and $(\omega_e - 2\alpha_e)$, respectively, *only if* accurate knowledge of the v' labels are available. In this work, we rely on finding potential parameters that reproduce the trends in the line strengths to unambiguously assign the levels as $v' = 5$–7, 23–26, as described in the main text. With this at hand, we extract $B_e = 0.021933(3)\,\mathrm{cm}^{-1}$ and $\omega_e = 83.528(13)\,\mathrm{cm}^{-1}$.

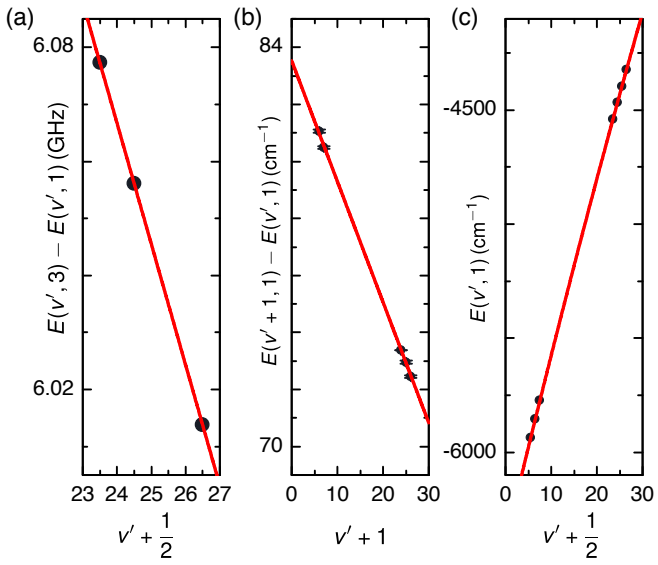

Figure S2. (a) Rotational splittings between $J' = 3$ and 1. (b) Adjacent vibrational splittings of $J' = 1$. (c) Binding energies of $J' = 1$. All states belong to the 1_u potential. The red lines are fits to the data: a linear function in (a) and (b), and a quadratic function in (c). The intercepts with the vertical axis are $10B_e$, $\omega_e - 2\alpha_e$, and $2B_e - D_e$ respectively. Error bars are 1σ uncertainties in (b), and are much smaller than the symbol size in (a) and (c).

The equilibrium bond length is then calculated using $R_e = \frac{1}{2\pi}\sqrt{\frac{h}{2\mu c B_e}} = 7.9027(5)\,a_0$.

The actual potential depth, D_e, relative to $^1S_0$-$^3P_1$ will be overestimated by the standard formula $\omega_e^2/4\omega_e x_e$ as the simple Morse model does not extrapolate well to the long-range. Instead, we determine D_e by fitting the binding energies versus $v'+\frac{1}{2}$ to Eq. (S10), with α_e, $\omega_e x_e$, and ω_e held fixed to the values above (see Fig. S2(c)). The vertical intercept of the quadratic fit will therefore be $2B_e - D_e$. Knowing B_e, we find $D_e = 6387.89(11)\,\mathrm{cm}^{-1}$.

CONSTRUCTION OF MORSE/LONG-RANGE POTENTIALS

The Morse/Long-range (MLR) potential as a function of internuclear separation R has the form

$$V_{\rm MLR}(R) = D_e \left[1 - \frac{u_{\rm LR}(R)}{u_{\rm LR}(R_e)} {\rm e}^{-\phi(R)\gamma_p(R)}\right]^2, \quad \text{(S13)}$$

where

$$u_{\rm LR}(R) = -\frac{C_3}{R^3} - \frac{C_6}{R^6} - \frac{C_8}{R^8} - \frac{C_{10}}{R^{10}}, \quad \text{(S14)}$$

$$\phi(R) = [1 - \gamma_p^{\rm ref}(R)] \sum_{i=0}^{N} (\gamma_q^{\rm ref}(R))^i \phi_i + \gamma_p^{\rm ref}(R)\phi_\infty,$$

$$\phi_\infty = \ln\left(\frac{2D_e}{u_{\rm LR}(R_e)}\right),$$

$$\gamma_p(R) = \frac{R^p - R_e^p}{R^p + R_e^p},$$

$$\gamma_p^{\rm ref}(R) = \frac{R^p - R_{\rm ref}^p}{R^p + R_{\rm ref}^p}.$$

As a starting point of the fitting procedure, we used the *ab initio* results from Ref. [S9] with the long-range coefficients fixed to the best available values deduced from experiments and *ab initio* calculations: C_3 from Ref. [S10], C_6 and C_8 from Ref. [S11], and C_{10} from Ref. [S12]. The well depth D_e and the equilibrium distance R_e of the 1_u potential were fixed at their empirical values found in this work. The p, q and $R_{\rm ref}$ parameters were chosen according to suggestions from Ref. [S13]. In particular, p is an integer greater than $n_{\rm max} - n_{\rm min}$, where $n_{\rm min} = 3$ and $n_{\rm max} = 10$ are the lowest and the highest powers in the long range expansion $u_{LR}(R)$. Parameter q is a smaller integer, typically q = 2–4 while $R_{\rm ref}$ is chosen such as $R_{\rm ref}/R_e = 1.1 - 1.5$. Introduction of additional parameters q and $R_{\rm ref}$ instead of simply using p and R_e leads to a better potential fit achieved with smaller number of terms in the expansion of $\phi(R)$ in Eq. (S14). Then the parameters ϕ_i of the 1_u potential were refitted to match the shape of the Morse potential well near the minimum. Finally, the parameters ϕ_0, ϕ_1, ϕ_2 of the 1_u potential as well as the C_6 and C_8 long-range coefficients of both 0_u^+ and 1_u potentials were fitted to a range of experimental $J' = 1$ binding energies given in Table SIII. A simultaneous fit of the long-range coefficients for both 0_u^+ and 1_u potential curves was necessary to correctly describe the heavily Coriolis-mixed states $0_u^+(v' = -6, J' = 1)$ and $1_u(v' = -3, J' = 1)$. The resulting parameters are given in the upper half of Table SIV. For convenience, the spectroscopic constants found in the preceding section are also listed in the lower half of Table SIV.

Table SIII. Binding energies for the bound states of 0_u^+ and 1_u, in units of MHz. Negative vibrational quantum numbers count down from the dissociation limit. The v' assignments for the deeply bound 1_u states are explicitly described as belonging to either the MLR or the *ab initio* (AI) potential. For the values obtained in this work, those of $1_u(v' = 23, 24, 26, J' = 1, 3)$ were determined via an optical frequency comb referenced to a NIST-traceable Rb standard, while the others were deduced with a commercial wavemeter. The uncertainty in the absolute binding energy of X($v = 6, J = 2$) at 25.070,581,141(76) THz dominates the uncertainty for the former, while the resolution of the wavemeter dominates for the latter. We use the $^1S_0$-$^3P_1$ intercombination-transition frequency from Ref. [S14].

State	v'	J'	*Ab initio* (AI)	MLR	Experiment	Ref.
0_u^+	-1	1	0.4438	0.4151	0.4653(45)	[S15]
0_u^+	-2	1	23.8652	23.7511	23.9684(59)	[S16]
0_u^+	-3	1	223.967	221.643	222.161(35)	[S17]
0_u^+	-4	1	1,087.732	1,083.751	1,084.093(33)	[S17]
0_u^+	-5	1	3,421.12	3,463.63	3,463.28(33)	[S17]
0_u^+	-6	1	8,038.76	8,429.56	8,429.65(42)	[S17]
1_u	-1	1	356.429	352.657	353.236(35)	[S17]
1_u	-2	1	2,686.905	2,684.103	2,683.722(32)	[S17]
1_u	-3	1	8,209.159	8,200.040	8,200.163(39)	[S17]
1_u	26 (MLR), 22 (AI)	1	129,004,636	129,586,955	129,584,289.647(761)	This work
1_u	25 (MLR), 21 (AI)	1	131,207,700	131,758,225	131,757,586(300)	This work
1_u	24 (MLR), 20 (AI)	1	133,424,436	133,942,696	133,943,814.291(763)	This work
1_u	23 (MLR), 19 (AI)	1	135,654,750	136,140,364	136,143,325.578(761)	This work
1_u	7 (MLR), 3 (AI)	1	173,112,867	173,081,203	173,083,976(300)	This work
1_u	6 (MLR), 2 (AI)	1	175,560,325	175,498,791	175,496,706(300)	This work
1_u	5 (MLR), 1 (AI)	1	178,019,781	177,928,703	177,926,824(300)	This work
1_u	26 (MLR), 22 (AI)	3	128,998,655	129,580,953	129,578,275.914(761)	This work
1_u	24 (MLR), 20 (AI)	3	133,418,411	133,936,648	133,937,758.133(762)	This work
1_u	23 (MLR), 19 (AI)	3	135,648,703	136,134,293	136,137,248.303(764)	This work

Table SIV. Morse/Long-range parameters of the $(1)0_u^+$ and $(1)1_u$ potentials in specified units. Also listed are the spectroscopic constants determined from the energies of deeply bound 1_u states.

	0_u^+	1_u
R_e (a_0)	7.5443	7.9027
D_e (cm^{-1})	2784	6388
C_3 ($E_h a_0^3$)	1.5235661×10^{-2}	7.6178307×10^{-3}
C_6 ($E_h a_0^6$)	3.8947894×10^{3}	4.0390241×10^{3}
C_8 ($E_h a_0^8$)	4.5157846×10^{5}	7.7660490×10^{5}
C_{10} ($E_h a_0^{10}$)	3.296×10^{7}	1.3253×10^{8}
p	9	9
q	4	4
R_{ref} (a_0)	8.2987	8.6930
ϕ_0	-0.63810976	-1.2454828
ϕ_1	3.5917033	-0.19418436
ϕ_2	7.7175691	-1.8890781
ϕ_3	0.57800325	-3.1121912
ϕ_4	-29.3700406	-6.0245946
ϕ_5	-23.080778	-5.6268047
ϕ_6	54.044018	-3.3425721
ϕ_7	91.862114	-0.0028626398
ϕ_8	35.061649	0
ϕ_9	-2.9283029	0
$\omega_e x_e$ (cm^{-1})	-	0.21150(28)
ω_e (cm^{-1})	-	83.528(13)
B_e (cm^{-1})	-	0.021933(3)
α_e (cm^{-1})	-	$7.068(11) \times 10^{-5}$

* Present address: Helmholtz-Institut Mainz, Johannes Gutenberg University, 55128 Mainz, Germany.
† Present address: Morgan Stanley, 1585 Broadway, New York, NY 10036, USA.
‡ Present address: Atom Computing, Inc., 918 Parker Street, Berkeley, CA 94710, USA.
§ tanya.zelevinsky@columbia.edu

[S1] G. Reinaudi, C. Osborn, M. McDonald, S. Kotochigova, and T. Zelevinsky, Optical production of stable ultracold $^{88}Sr_2$ molecules, Phys. Rev. Lett. **109**, 115303 (2012).

[S2] J. Stenger, H. Schnatz, C. Tamm, and H. R. Telle, Ultraprecise measurement of optical frequency ratios, Phys. Rev. Lett. **88**, 073601 (2002).

[S3] N. Scharnhorst, J. B. Wübbena, S. Hannig, K. Jakobsen, J. Kramer, I. D. Leroux, and P. O. Schmidt, High-bandwidth transfer of phase stability through a fiber frequency comb, Opt. Express **23**, 19771 (2015).

[S4] M. McDonald, B. H. McGuyer, G. Z. Iwata, and T. Zelevinsky, Thermometry via light shifts in optical lattices, Phys. Rev. Lett. **114**, 023001 (2015).

[S5] B. H. McGuyer, M. McDonald, G. Z. Iwata, M. G. Tarallo, W. Skomorowski, R. Moszynski, and T. Zelevinsky, Precise study of asymptotic physics with subradiant ultracold molecules, Nat. Phys. **11**, 32 (2015).

[S6] R. Bause, M. Li, A. Schindewolf, X.-Y. Chen, M. Duda, S. Kotochigova, I. Bloch, and X.-Y. Luo, Tune-out and magic wavelengths for ground-state $^{23}Na^{40}K$ molecules, Phys. Rev. Lett. **125**, 023201 (2020).

[S7] S. G. Porsev, A. D. Ludlow, M. M. Boyd, and J. Ye, Determination of Sr properties for a high-accuracy optical clock, Phys. Rev. A **78**, 032508 (2008).

[S8] I. Ushijima, M. Takamoto, and H. Katori, Operational magic intensity for Sr optical lattice clocks, Phys. Rev. Lett. **121**, 263202 (2018).

[S9] W. Skomorowski, F. Pawłowski, C. P. Koch, and R. Moszynski, Rovibrational dynamics of the strontium molecule in the $A^1\Sigma_u^+$, $c^3\Pi_u$, and $a^3\Sigma_u^+$ manifold from state-of-the-art ab initio calculations, J. Chem. Phys. **136**, 194306 (2012).

[S10] M. Borkowski, P. Morzyński, R. Ciuryło, P. S. Julienne, M. Yan, B. J. DeSalvo, and T. C. Killian, Mass scaling and nonadiabatic effects in photoassociation spectroscopy of ultracold strontium atoms, Phys. Rev. A **90**, 032713 (2014).

[S11] S. G. Porsev, M. S. Safronova, and C. W. Clark, Relativistic calculations of C_6 and C_8 coefficients for strontium dimers, Phys. Rev. A **90**, 052715 (2014).

[S12] J. Mitroy and J. Zhang, Dispersion and polarization interactions of the strontium atom, Mol. Phys. **108**, 1999 (2010).

[S13] R. J. Le Roy, N. S. Dattani, J. A. Coxon, A. J. Ross, P. Crozet, and C. Linton, Accurate analytic potentials for $Li_2(X^1\Sigma_g^+)$ and $Li_2(A^1\Sigma_u^+)$ from 2 to 90 Å, and the radiative lifetime of $Li(2p)$, J. Chem. Phys. **131**, 204309 (2009).

[S14] G. Ferrari, P. Cancio, R. Drullinger, G. Giusfredi, N. Poli, M. Prevedelli, C. Toninelli, and G. M. Tino, Precision frequency measurement of visible intercombination lines of strontium, Phys. Rev. Lett. **91**, 243002 (2003).

[S15] M. McDonald, *High precision optical spectroscopy and quantum state selected photodissociation of ultracold* $^{88}Sr_2$ *molecules in an optical lattice* (Springer, 2017).

[S16] B. McGuyer, M. McDonald, G. Z. Iwata, M. Tarallo, A. Grier, F. Apfelbeck, and T. Zelevinsky, High-precision spectroscopy of ultracold molecules in an optical lattice, New J. Phys. **17**, 055004 (2015).

[S17] T. Zelevinsky, M. M. Boyd, A. D. Ludlow, T. Ido, J. Ye, R. Ciuryło, P. Naidon, and P. S. Julienne, Narrow line photoassociation in an optical lattice, Phys. Rev. Lett. **96**, 203201 (2006).